The Spectre Realized on Artificial Graphene

Connor Blake, Pierre Darancet

September 12, 2023

1 Aperiodic Tiling: The Spectre

1.1 Spectre Connectivity Rules

Discovered in May 2023 (Smith et al., 2023), the Spectre is the first aperiodic chiral monotile which can tile the plane. While Tile (1,1) permits periodic tilings using its reflection, a chiral edge modification allows only aperiodic tilings and is referred to as "the Spectre". However, we are only interested in the aperiodic graph properties, so we will refer to the tiling as "the Spectre" regardless of edge modifications. The Spectre has 14 edges of equal length and 14 vertices (Figure 1). The Spectre's tiling forms a bipartite graph, with one lattice having coordination numbers of two, three, and four (A sublattice, angles in multiples of 90°) and the other having coordination numbers of two and three (B sublattice, angles in multiples of 120°) (Figure 2). There are an equal number of A and B sites on any given tiling of the Spectre composed of metatiles, and each sublattice has the same average coordination.

As with any aperiodic tiling, the inflation rules are key to understanding the patterns in the graph. The Spectre has 9 meta tiles Γ through Ψ. Excluding the Γ metatile, each metatile is identical (Figure 6) and only differs in the way its edges are permitted to connect. The edge labelling scheme as adopted in the original paper is shown in Figure 4. There are eight types of edge connection, α through θ. Each matches with its opposite polarity (e.g. $\alpha+$ with $\alpha-$) except for η which matches with itself. Each metatile (Figure 4) forms into clusters of the same labelling scheme (Figure 5), and the Spectre shape itself makes up the metatiles as shown in Figure 6. Each collection of connected metatiles is referred to as a"patch", either in the vertex form or metatile form (Figure 3). Note that between recursion levels, the Spectre shape and thus tiles undergo a reflection about their orientation axes (a line from the top left corner to the bottom right through each letter in Figure 4).

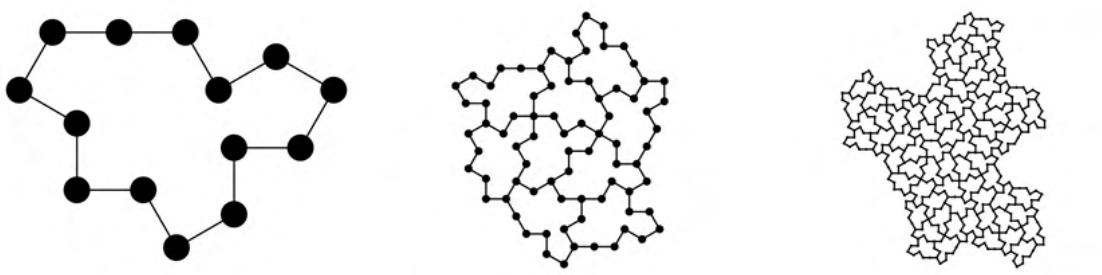

(a) Recursion Level 0 (b) Recursion Level 1 (c) Recursion Level 2

Figure 1: The base Spectre and higher order tilings. The shape is equilateral with angles in multiples of 90°or 120°. The first recursion level (Figure 1b) of the individual Spectre shape is what we will subsequently refer to as a "tile" or "metatile". Shown here is a non-Γ tile. The second recursion level (Figure 1c) shows a cluster of metatiles. All such clusters can be seen in Figure 5.

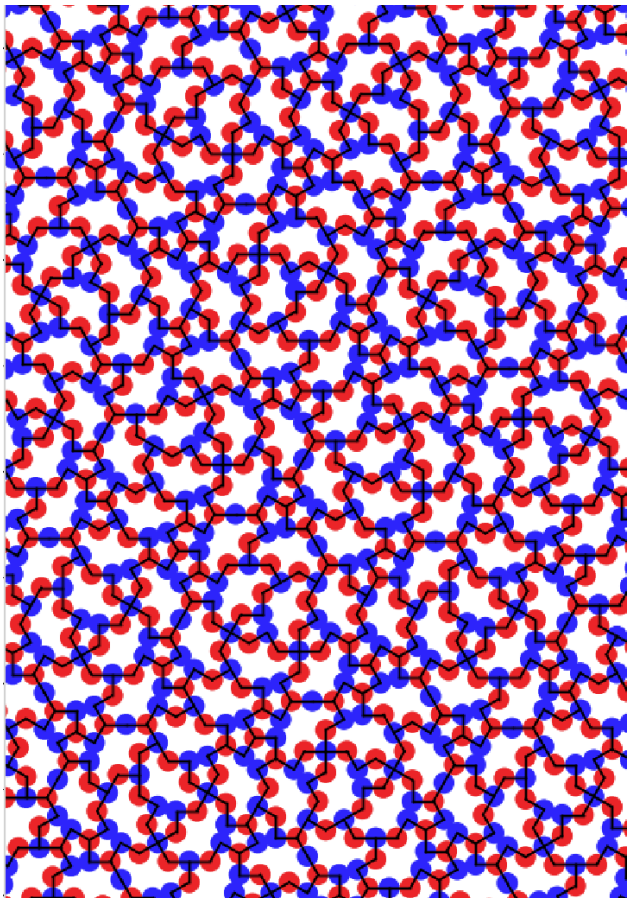

Figure 2: A large tiling of Spectre shapes marked according to their sublattice. A sublattice is in blue, and B sublattice is in red.

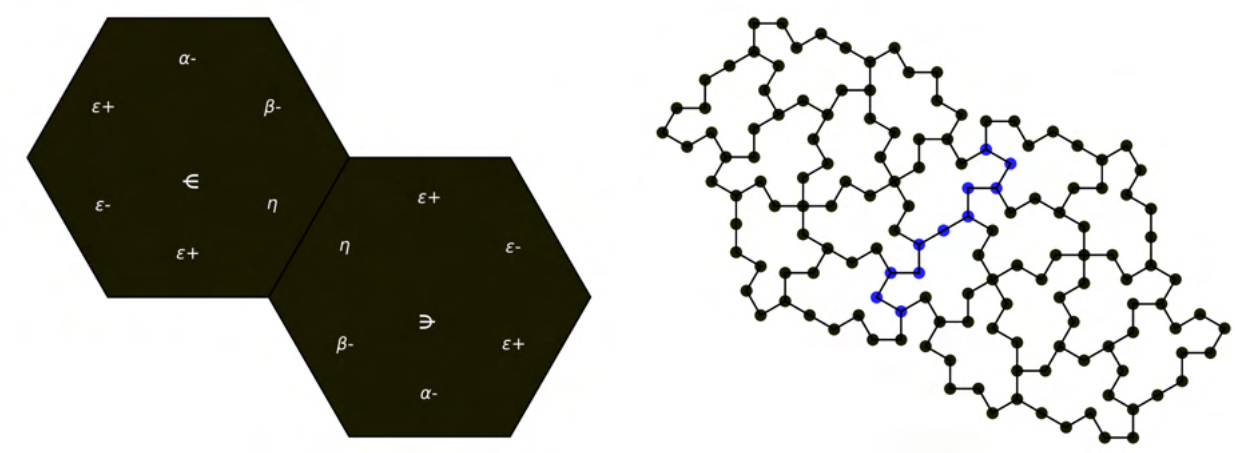

(a) Metatiles: Two Psi metatiles connected along an η edge.

(b) Vertices: The same metatiles in vertex form. The blue vertices denote the shared η edge.

Figure 3: Ψ-Ψ Patch in metatile and vertex forms.

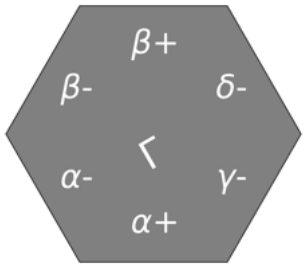

(a) Gamma Tile

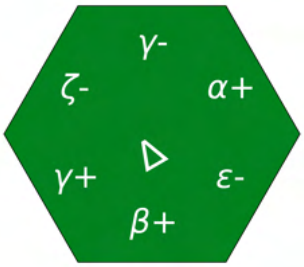

(b) Delta Tile

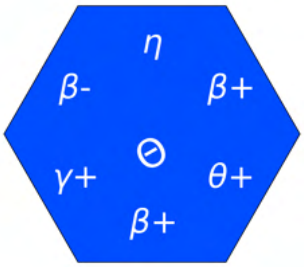

(c) Theta Tile

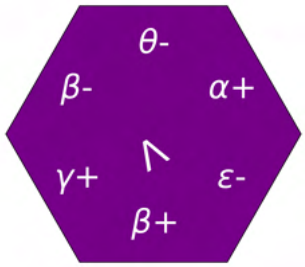

(d) Lambda Tile

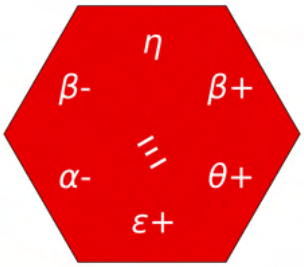

(e) Xi Tile

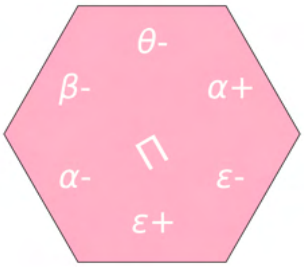

(f) Pi Tile

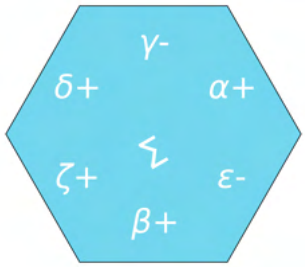

(g) Sigma Tile

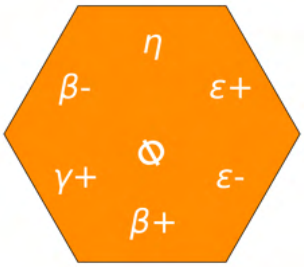

(h) Phi Tile

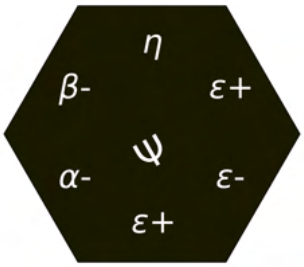

(i) Psi Tile

Figure 4: Metatiles with labelled edges.

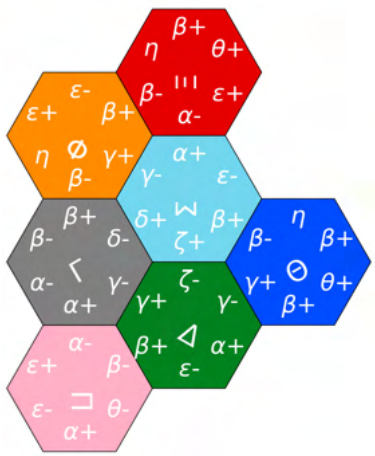

(a) Gamma Cluster

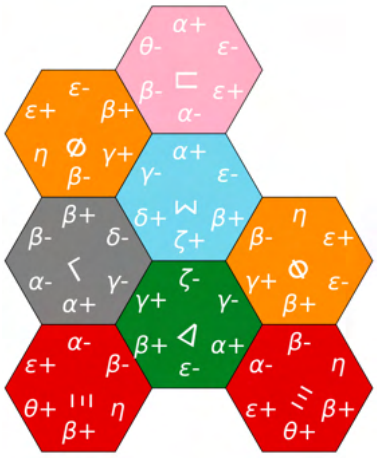

(b) Delta Cluster

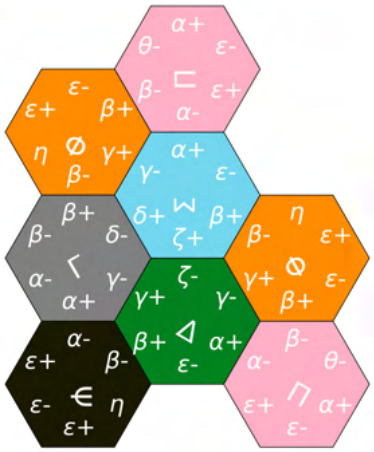

(c) Theta Cluster

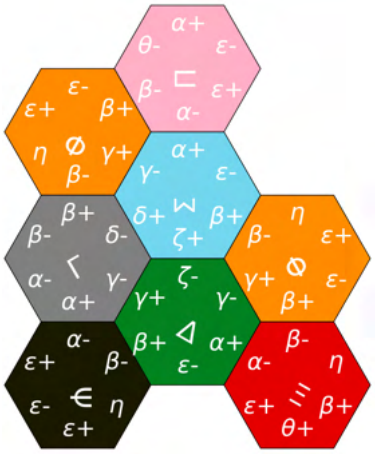

(d) Lambda Cluster

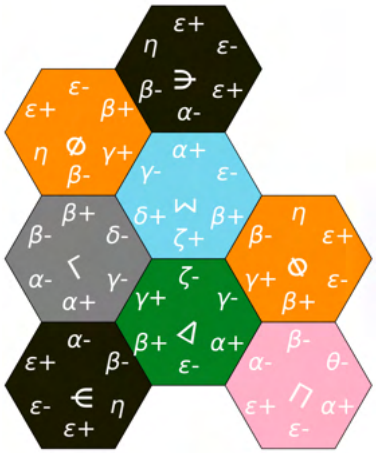

(e) Xi Cluster

(f) Pi Cluster

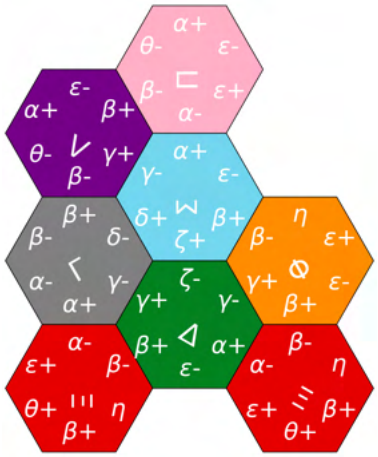

(g) Sigma Cluster

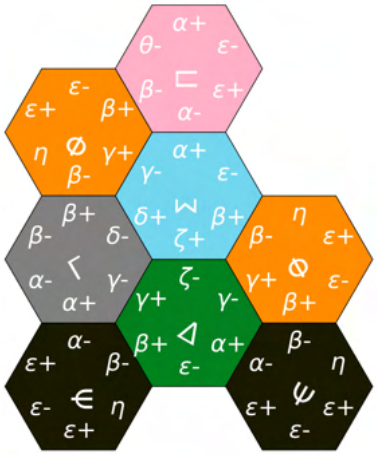

(h) Phi Cluster

(i) Psi Cluster

Figure 5: Metatile clusters.

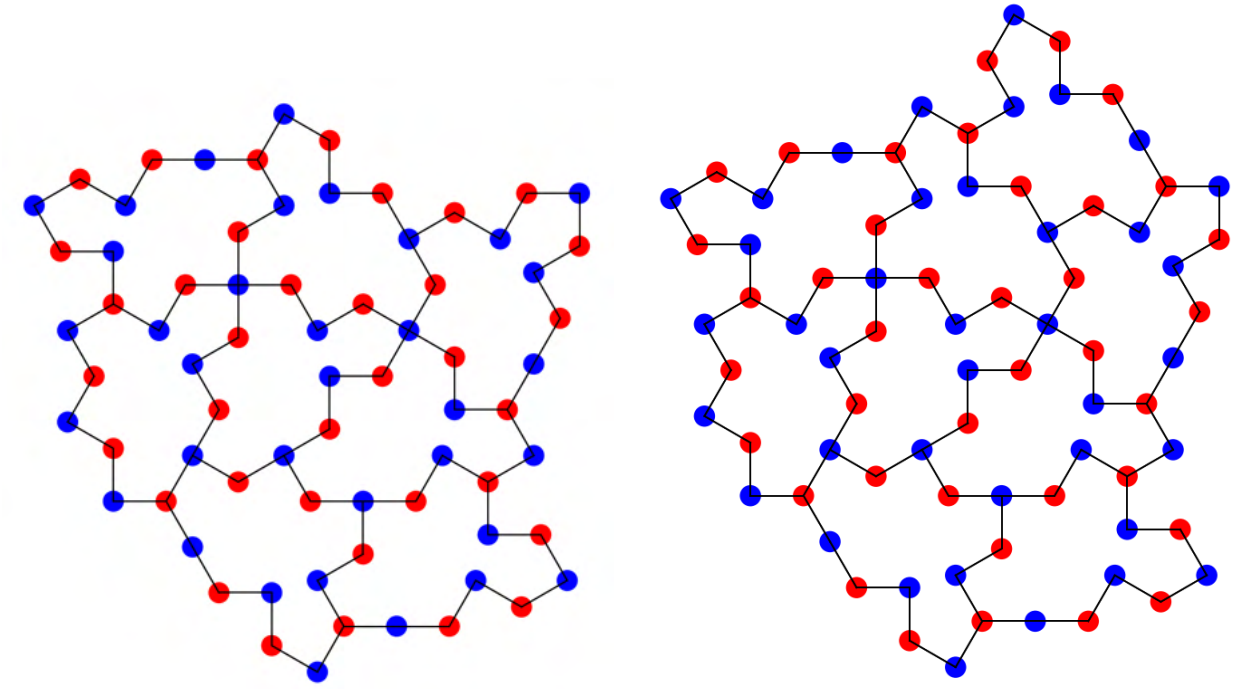

(a) The Γ metatile in vertex form.

(b) All other metatiles in vertex form.

Figure 6: Metatile representations in vertex form.

1.2 Quasicrystal Background

We use various forms of tight binding models to study the Spectre. While Schirmann et al., 2023 has studied the Hat and Spectre in some detail with a similar tight-binding model, our models are not equivalent. While they primarily consider the Hat, a shape with two side-lengths that does require reflections in the plane, they also treat the graph differently. Their model uses three side-lengths (and presumably 2 in the Spectre, though they do not specify), counting a 180° vertex as a single, longer straight line. An example of this kind of 180° vertex can be seen in the exact center of Figure 3b. Crucially, their decision to consider three different edge-lengths renders their graph non-bipartite. This long-edge decision also has the consequence of making certain metatiles non unique, a feature which will be key to our further analysis. While Schirmann et al., 2023 only studies a single inflation of the Hat, H2, we argue that the most important properties which emerge in the Spectre only exist in the interplay between inflation levels of metatiles.

Though individual vertices of Spectres do not align with a hexagonal lattice, the simulated diffraction pattern of a large patch shows strong 12-fold symmetry (Figure 7), indicative of an underlying hexagonal structure of the tiling.

The Spectre is not the first aperiodic lattice with hexagonal character to be studied. Socolar and Taylor, 2011 presents a monotile and its reflection which aperiodically tile the plane, but its properties do not appear to have received any attention in the quasicrystal literature. Matsubara et al., 2023 explores a class of hexagonal golden-mean aperiodic lattices using a tight-binding model. Similar to the Spectre, their graphs are bipartite and have multiple coordination numbers per sublattice. However, they are comprised of multiple shapes, have a sublattice imbalance (Koga and Coates, 2022), and have multiple kinds of edge-lengths.

One typical method of understanding aperiodic lattices is the cut-and-project method which projects a higher dimensional periodic lattice onto fewer dimensions, thus losing its periodicity. While both the hexagonal golden-mean lattice (Coates et al., 2023) and Taylor-Socolar tilings (Lee and Moody, 2012) can be understood in terms of a cut-and-project method, the authors of the Spectre do not attempt to identify such a method. Socolar, 2023 outlines such a system for describing the Hat, but it remains to be seen how the Spectre might be understood in this way because the Hat and Spectre have different inflation patterns

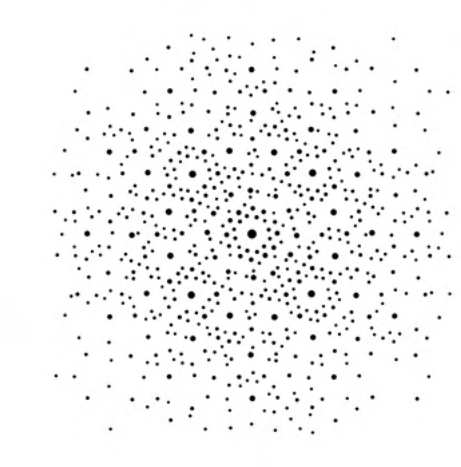

Figure 7: Discrete Fourier transform on a patch with 2219 vertices.

despite coming from the same polykite family.

Unlike other bipartite aperiodic lattices such as the Penrose lattice, Ammann-Beenker lattice, Socolar dodecagonal lattice, and hexagonal golden-mean tiling, we observe relatively few zero-modes. While zero-modes in the Penrose lattice comprise nearly 10% of the spectrum (Arai et al., 1988) and large percentages in the others (Matsubara et al., 2023), we observe no meaningful scaling law between the size of the patch and the number of zero-modes. We examine zero-modes and other mid-spectrum modes in Section 1.7.

1.3 Our Models

The Spectre "vertex" model uses the aforementioned bipartite graph and sets all hopping terms to one with zero onsite energy. This Hamiltonian is equivalent to the negative graph adjacency matrix.

The Spectre "meta-vertex" model gives each metatile in a patch N_{meta} "orbitals". These orbitals correspond to the first N_{meta} eigenvalues of the individual metatile wave functions. For example, the first eigenstate of a non-Γ metatile is shown in Figure 9a. The hopping terms correspond to the kinetic energy overlap between two adjacent tile states, and the onsite energies correspond to those states' respective energies. We find that only one eigenstate per metatile serves as a good approximation to the first N_{tiles} states of the vertex model.

In the "super-vertex" model we use only the first eigenstate of each metatile to construct a tight binding Hamiltonian on a periodic triangular lattice of metatiles. In this model, each site is classified as either Γ or non-Γ for its onsite energy and has hopping terms determined by relative orientation and Γ-character of its neighbors. We find that this ansatz serves as a good approximation to large vertex models and demonstrates self-similarity.

1.4 Vertex Model

1.4.1 Definitions

Our vertex Hamiltonian equation has the standard nearest-neighbor form

$$H_{\text{tot}} = -t \sum_{\langle i \,|\, j \rangle} \left(c_i^\dagger c_j + c_j^\dagger c_i \right) \tag{1}$$

where $\langle i \,|\, j \rangle$ is one for all nearest neighbors and zero otherwise. The full set of vertices $\{|i\rangle\}$ defines our Hilbert space $\mathcal{H}^{N_{\text{orb}}}(\mathbb{C})$. Our N_{orb} states over the whole patch are then given by

$$H_{\text{tot}} \, |\Psi_{\text{tot}}^n\rangle = E_{\text{tot}}^n \, |\Psi_{\text{tot}}^n\rangle \tag{2}$$

The first eigenstates of various patches can be seen in Figure 9. The density of states of both the patch shown in Figure 3 and Figure 10 can be seen in Figure 8. Note that both spectra are symmetric because all vertex model graphs are bipartite. On a hexagonal patch of seven tiles, we notice strong localization around each tile's two four-coordinated vertices in a density map of the first n electrons filling a patch (Figure 10). These images serve as motivation for all subsequent models. From here we aim to reduce the computational complexity of the model while preserving its key features and the underlying complex symmetries.

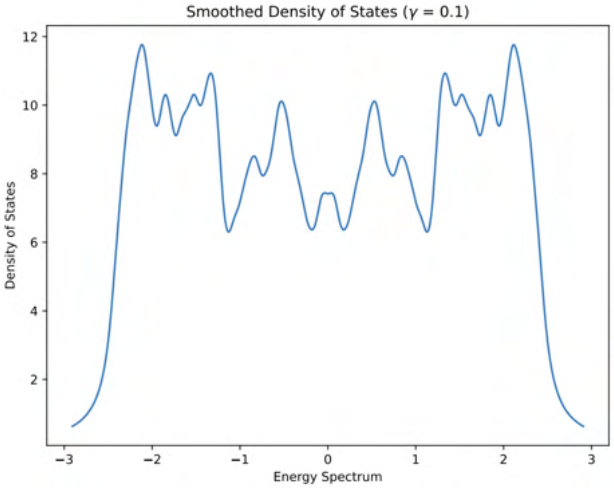

(a) Density of states of the Ψ-Ψ patch from Figure 3.

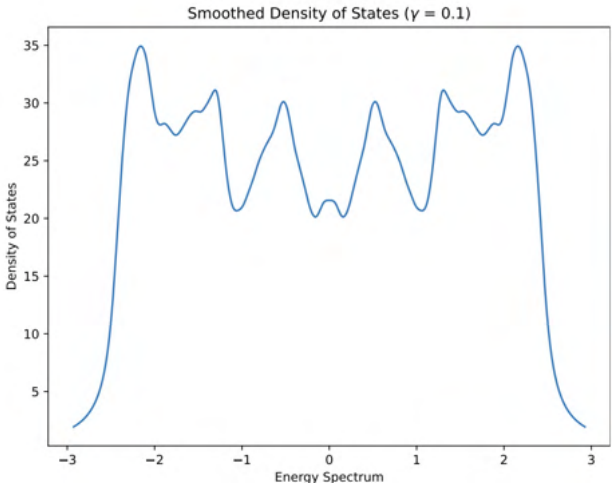

(b) Density of states of the 7-metatile patch from Figure 10.

Figure 8: Density of states plot for patches of 2 and 7 tiles respectively. These graphs and all subsequent density of states (DOS) graphs are smoothed according to a Lorentzian distribution with a specified γ parameter. As is known from spectral graph theory, the maximum eigenvalue (lowest energy) represents the average coordination number in the graph, around 2.4 for both of these patches.

1.5 Meta-vertex Model

The purpose of this model is to see how well the states of the vertex model can be captured by a model that places N_{meta} orbitals on each of the N_{tiles}. This effectively reduces the size of the Hamiltonian from N_{orb} ($\sim 75N_{\text{tiles}}$) to $N_{\text{tiles}}N_{\text{meta}}$. To do so, we introduce a set of non-orthogonal projectors for each tile in $\{A\}$. A table of symbols and explanations can be found in Table 1.

$$P_A = \sum_{i_A}^{\dim |i\rangle_A} |i_A\rangle \langle i_A| \tag{3}$$

These projectors have the property $\text{tr}(P_A) = N_A$. Because each tile shares vertices with its six neighbors, the projectors also obey the relation:

$$\mathbf{I} = \sum_{A}^{\{A\}} P_A - \sum_{A}^{\{A\}} \sum_{B<A}^{\{B\}} P_A P_B + \sum_{A}^{\{A\}} \sum_{B<A}^{\{B\}} \sum_{C<A,B}^{\{C\}} P_A P_B P_C \tag{4}$$

Each tile state, $|\Psi_A^n\rangle$, is defined in the following way:

$$P_A H_{\text{tot}} P_A |\Psi_A^n\rangle = E_A^n |\Psi_A^n\rangle \tag{5}$$

The meta-vertex model only considers the first N_{meta} of these N_A eigenstates. A new Hamiltonian can now be described in the $|\Psi_A^n\rangle$ basis as follows:

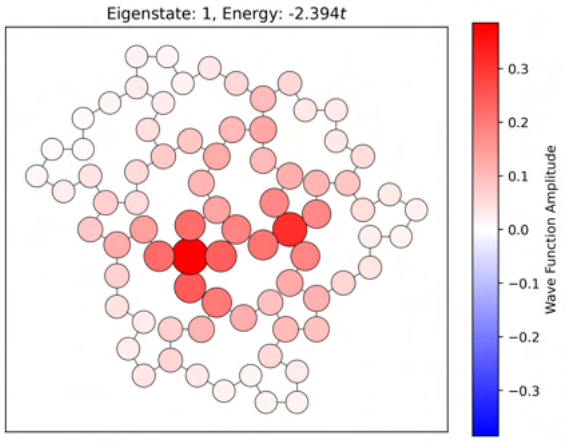

(a) First eigenstate of a non-Γ metatile. This is referred to as recursion level 1.

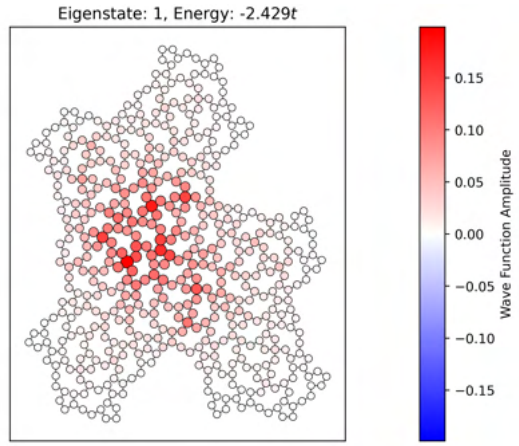

(b) First eigenstate of a non-Γ metatile recursion level 2.

Figure 9: First eigenstate of various patch sizes.

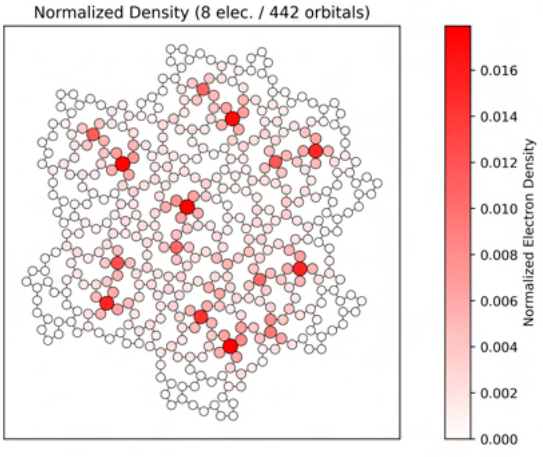

(a) Normalized electron density with eight electrons.

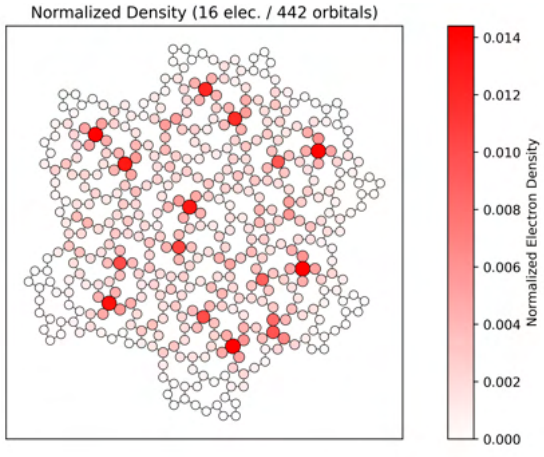

(b) Normalized electron density with 16 electrons.

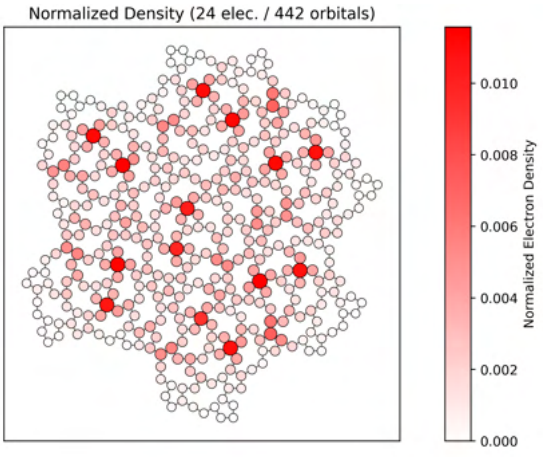

(c) Normalized electron density with 24 electrons.

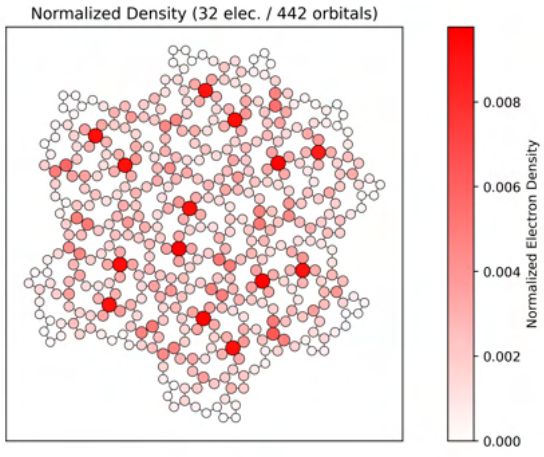

(d) Normalized electron density with 32 electrons.

Figure 10: Normalized probability density map of the first n electrons of a patch of seven metatiles.

451	-2.394	0	-0.072	-0.069	0	0	0	0	0	0	-0.024	-0.029	-0.017	0
451	0	-2.306	-0.101	-0.094	0	0	0	0	0	0	0	0	-0.008	0
462	-0.072	-0.101	-2.394	0	-0.024	0	0	0	0	0	0	0	-0.009	0
462	-0.069	-0.094	0	-2.306	-0.03	0	0	0	0	0	0	0	-0.016	0
461	0	0	-0.024	-0.03	-2.394	0	-0.097	-0.04	0	0	0	0	-0.05	-0.054
461	0	0	0	0	0	-2.306	-0.164	-0.052	0	0	0	0	-0.051	-0.066
464	0	0	0	0	-0.097	-0.164	-2.39	0	-0.016	-0.012	0	0	-0.02	-0.037
464	0	0	0	0	-0.04	-0.052	0	-2.304	0	0	0	0	0	0
449	0	0	0	0	0	0	-0.016	0	-2.394	0	-0.009	-0.009	-0.063	-0.071
449	0	0	0	0	0	0	-0.012	0	0	-2.306	0	0	0	0
450	-0.024	0	0	0	0	0	0	0	-0.009	0	-2.394	0	-0.033	0
450	-0.029	0	0	0	0	0	0	0	-0.009	0	0	-2.306	-0.046	0
463	-0.017	-0.008	-0.009	-0.016	-0.05	-0.051	-0.02	0	-0.063	0	-0.033	-0.046	-2.394	0
463	0	0	0	0	-0.054	-0.066	-0.037	0	-0.071	0	0	0	0	-2.306

Figure 11: Example of H_{meta} for $N_{\text{meta}} = 2$ for the tile shown in Figure 12.

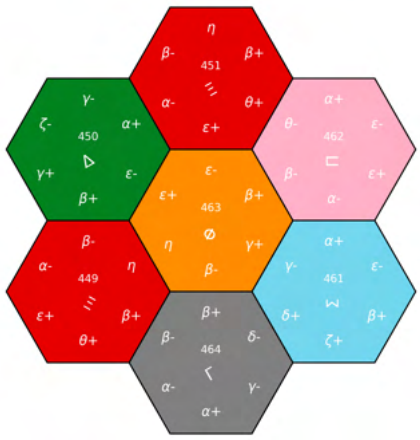

Figure 12: Patch of 7 tiles

$$H_{\text{meta}} = \sum_{A}^{\{A\}} \sum_{B}^{\{B\}} \sum_{n}^{N_{\text{meta}}} \sum_{m}^{N_{\text{meta}}} |\Psi_A^n\rangle \langle\Psi_A^n| H_{\text{tot}} |\Psi_B^m\rangle \langle\Psi_B^m| \tag{6}$$

Thus the diagonal of H_{meta} is formed by N_{tiles} blocks of size N_{meta} by N_{meta}, each equivalent to $\langle\Psi_A^n| H_{\text{tot}} |\Psi_A^m\rangle = E_A^n \delta_{nm}$. An example of a Hamiltonian of this type where $N_{\text{meta}} = 2$ for a patch of 7 tiles can be seen in Figure 11. The far left column indicates the tile index as labelled in Figure 12.

We now solve for the eigenfunctions of H_{meta}. The eigenstates will be represented by $|\alpha^n\rangle$. Its first N_{meta} coefficients correspond to the coefficients of the eigenstates of $|\Psi_A\rangle$, the next N_{meta} to $|\Psi_B\rangle$ and so on. We must also use an overlap matrix S to capture the non-orthogonality of $|\Psi_A\rangle$ and $|\Psi_B\rangle$ which takes the form:

$$S = \sum_{A}^{\{A\}} \sum_{B}^{\{B\}} \sum_{n}^{N_{\text{meta}}} \sum_{m}^{N_{\text{meta}}} |\Psi_A^n\rangle \langle\Psi_A^n | \Psi_B^m\rangle \langle\Psi_B^m| \tag{7}$$

Now we solve for the eigenstates $|\alpha^n\rangle$:

$$H_{\text{meta}} |\alpha^n\rangle = E_{\text{meta}}^n S |\alpha^n\rangle \tag{8}$$

While these states are difficult to visualize, we noticed that the $(nN_{\text{meta}} + 1)^{th}$ $(n \in \{0, \ldots, N_{\text{tiles}} - 1\})$ coefficients of $|\alpha^n\rangle$ were the largest. This led us to propose the following hypothesis: **The first N_{tiles} eigenstates of H_{tot}can be described solely the first eigenstate of each tile in the patch.**

In order to judge how well this model describes the eigenstates of H_{tot}, we compute the the probability weight of a single tile A in the n^{th} state of $|Psi_{\text{tot}}\rangle$. We define the "tile norm" for some state n of A as:

$$T_{A,n} = \sum_{m}^{N_A} |\langle\Psi_{\text{tot}}^n | \Psi_A^m\rangle|^2 \tag{9}$$

We then define the "state-n, m completeness of A" as:

$$C_{A,n,m} = \frac{|\langle \Psi^n_{\text{tot}} \mid \Psi^m_A \rangle|^2}{T_{A,n}} \tag{10}$$

$C_{A,n,m}$ describes how much of the overlap of $|\Psi^n_{\text{tot}}\rangle$ with tile $|\Psi_A\rangle$ is accounted for by the m^{th} state $|\Psi^m_A\rangle$. For our model to be validated, $C_{A,n,1} \approx 1$ $n \in 1, \ldots, N_A$. While the numbers shown in Figure 13 may not appear close enough to 1 to warrant this ansatz, $C_{A,n,m\neq 1}$ is generally much lower and somewhat evenly distributed up to about the N^{th}_{tiles} eigenstate.

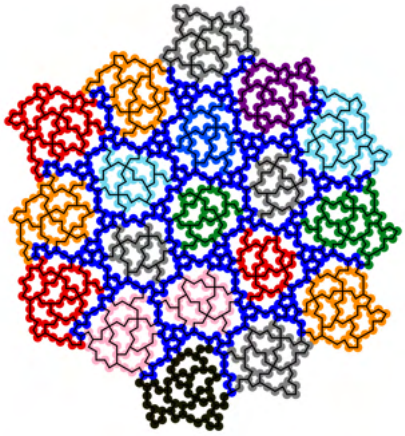

(a) Patch of 19 metatiles in vertex form.

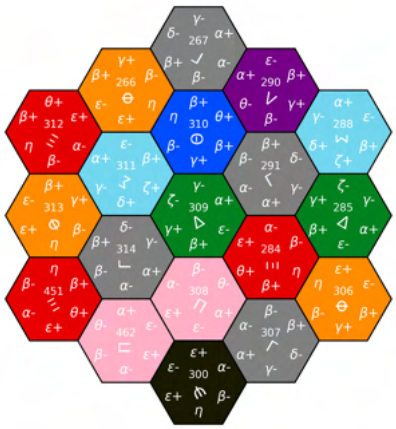

(b) Patch of 19 metatiles in metatile form.

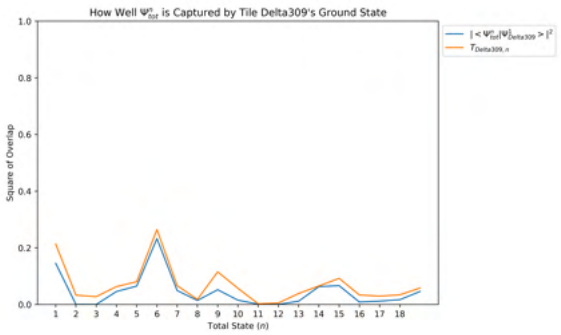

(c) Just considering the center tile, this graph demonstrates that for the first 19 (N_{tiles} eigenstates of the overall wave function $|\Psi_{\text{tot}}\rangle$, the center tile's weight in the wave function (orange) is closely captured by just the first eigenstate (blue) over a wide range of values.

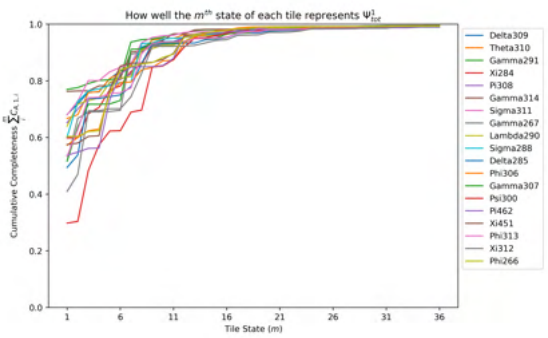

(d) This graph shows the cumulative completeness of each tile. It indicates that fewer than 10 eigenstates (of the total 71 or 78 per tile) are necessary to reconstruct the overall wave function to 90+% accuracy.

Figure 13: For a patch of 19 metatiles, these graphs indicate that the first eigenstate of each metatile makes up a significant contribution of each tile's contribution to the overall wave function.

1.6 Super-vertex Model

Now that we have established that the first eigenstates of each metatile capture the states of the full vertex model, we seek to further simplify the model by looking at only the metatiles. We now work on a 6-fold coordinated periodic triangular lattice with one "atomic orbital" on each site. Because each non-Γ metatile is identical in composition (but not connectivity), we propose a further ansatz: Each "orbital" has an onsite energy equal to E^1_Γ or $E^1_{\sim\Gamma}$. Each hopping term t_{AB} is fully determined by three variables. These are the

Symbol	Description
$\|i\rangle$	Orthonormal basis set formed by the N_{orb} "atomic" orbitals spanning the full Hilbert space.
$H_{\text{tot}} = \sum_{i,j}^{N_{\text{orb}}} \|i\rangle \langle i\| H_{\text{tot}} \|j\rangle \langle j\|$	H_{tot} will always be assumed in the $\|i\rangle$ basis unless described otherwise.
$\{A\}$	The set of all N_{tiles}.
$\|i\rangle_A$	The subspace associated with tile A of $\dim \|i\rangle_A = N_A \approx N_{\text{orb}}/N_{\text{tiles}}$. This is not an exact equality because the Γ metatile has 71 vertices while the rest have 78.
N_A	The number of vertices in tile A.

Table 1: Table of Symbol Definitions

relative orientations of the two tiles to their shared edge and whether either tile is Γ (there are no Γ-Γ pairings, and order does not matter). Searching across successively larger patches of metatiles, we find 15 unique "pairing" types (Figure 14). While there are 15 types of edges as laid out in the original paper $(\alpha+, \alpha-, \ldots, \eta)$ these only form eight kinds of "connections" $(\alpha, \beta, \ldots, \eta)$. Using values from H_{meta}, each of these pairing types has exactly one hopping energy across all patches and corresponds to exactly one type of "connection". The pairing connection types are not equally distributed: α has 3, β 4, γ 2, δ 1, ϵ 2, ζ 1, η 1, θ 1.

In other words, we are essentially arguing that

$$|\Psi^n_{\text{tot}}\rangle = \sum_A^{\{A\}} c_{A,n} \left|\Psi^1_A\right\rangle \tag{11}$$

is a good approximation for $n \in \{1 \ldots N_{\text{tiles}}\}$ where $c_{A,n}$ is some unknown coefficient.

Using the unique hopping and onsite terms from H_{meta}, we create a new Hamiltonian H_{super} on a new Hilbert space of the metatiles $\mathcal{H}^{N_{\text{tiles}}}(\mathbb{C})$, i.e. $\{|m\rangle\}$. (Note: this is different from the non-orthogonal "metatile eigenbasis" $\{|\Psi_A\rangle\}$ which is defined on the underlying $\{|i\rangle\}$ Hilbert space.)

Explicitly, the hopping terms t_{AB} are given by

$$t_{AB} = \left\langle \Psi^1_A \right| H_{\text{tot}} \left| \Psi^1_B \right\rangle \tag{12}$$

and the onsite energies ϵ_A are given by

$$\epsilon_A = \left\langle \Psi^1_A \right| H_{\text{tot}} \left| \Psi^1_A \right\rangle \tag{13}$$

The full Hamiltonian is then:

$$H_{\text{super}} = \sum_A^{\{A\}} \epsilon_A c^\dagger_A c_A - \sum_{\langle A \,|\, B\rangle}^{\{A\},\{B\}} t_{AB} \left(c^\dagger_A c_B + c^\dagger_B c_A \right) \tag{14}$$

We now solve for its eigenstates, $|\Psi_{\text{super}}\rangle$:

$$H_{\text{super}} \left|\Psi^n_{\text{super}}\right\rangle = E^n_{\text{super}} \left|\Psi^n_{\text{super}}\right\rangle \tag{15}$$

As a test case, we use a patch of 19 metatiles and visualize "what the electron sees" via colored triangles (Figure 15) representing t_{AB}.

To validate this test case, we compute both $|\Psi^n_{\text{tot}}\rangle$ and $\left|\Psi^n_{\text{super}}\right\rangle$ for $(n \in \{1, \ldots, N_{\text{tiles}}\})$. Selected examples are shown in Figure 17. We see that the full vertex modes which are highly asymmetric compared to an equal-hopping model are accurately captured in the H_{super} model. The DOS of this system can be seen in Figure 16.

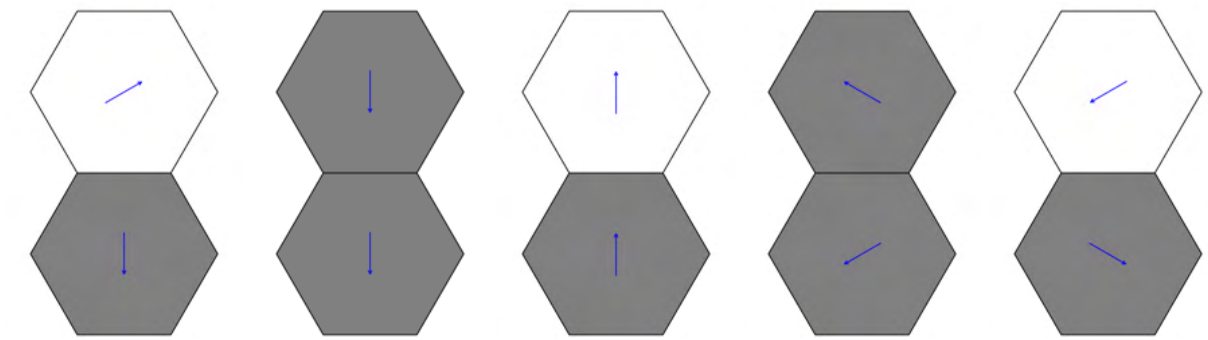

(a) α Pairing 1, $t_1 = -0.012$ (b) α Pairing 2, $t_2 = -0.024$ (c) α Pairing 3, $t_3 = -0.025$ (d) β Pairing 1, $t_4 = -0.009$ (e) β Pairing 2, $t_5 = -0.020$

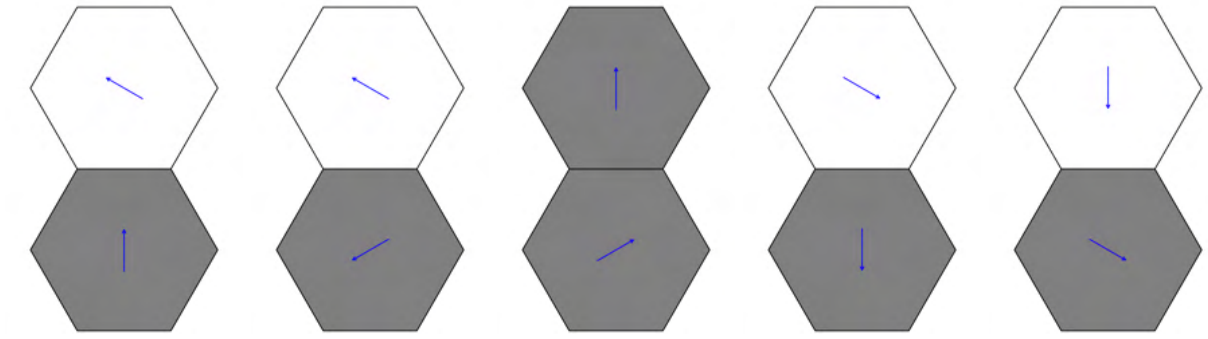

(f) β Pairing 3, $t_6 = -0.016$ (g) β Pairing 4, $t_7 = -0.009$ (h) γ Pairing 1, $t_8 = -0.050$ (i) γ Pairing 2, $t_9 = -0.051$ (j) δ Pairing, $t_{10} = -0.097$

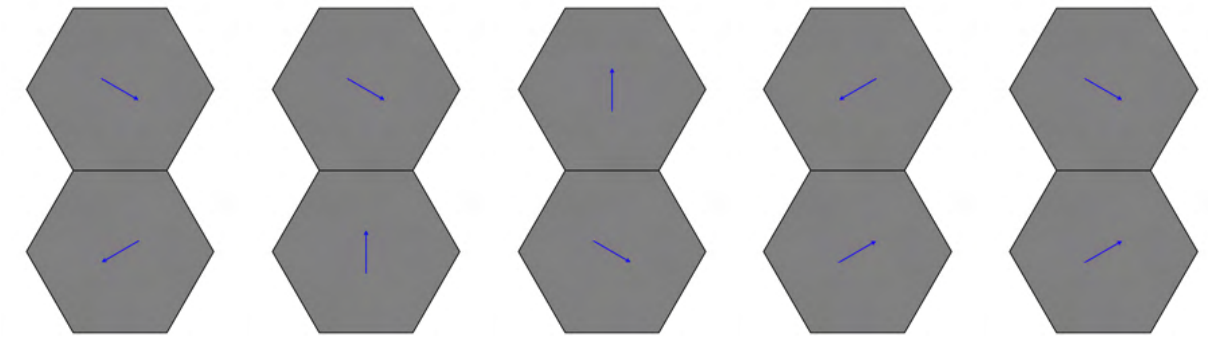

(k) ϵ Pairing 1, $t_{11} = -0.017$ (l) ϵ Pairing 2, $t_{12} = -0.033$ (m) ζ Pairing, $t_{13} = -0.072$ (n) η Pairing, $t_{14} = -0.063$ (o) θ Pairing, $t_{15} = -0.072$

Figure 14: All 15 pairing types. These pairings appear in any orientation within a sufficiently large patch. Grey represents non-Γ, white Γ. The arrow points in the orientation of the letter show in Figure 4. The t_i value for each corresponds to the overlap as computed by $\left\langle \Psi_A^1 \right| H_{\text{tot}} \left| \Psi_B^1 \right\rangle$. These values represent all off-diagonal terms in H_{super}.

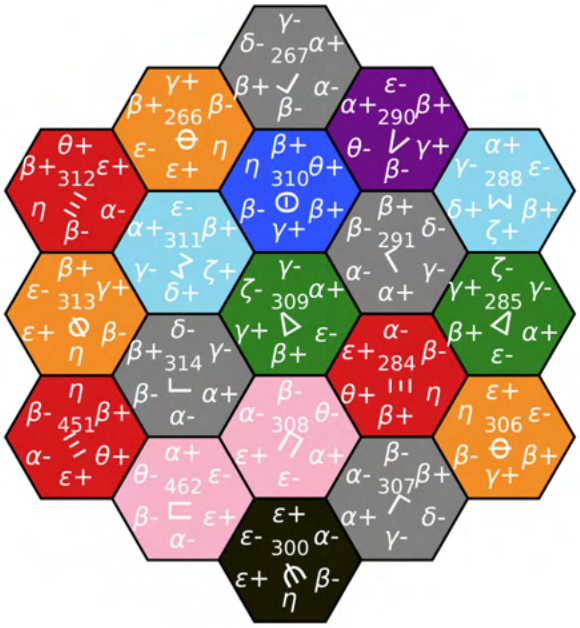

(a) Patch labelled by tile type and edge connection. (The numbers are for patch indexing and have no other meaning.

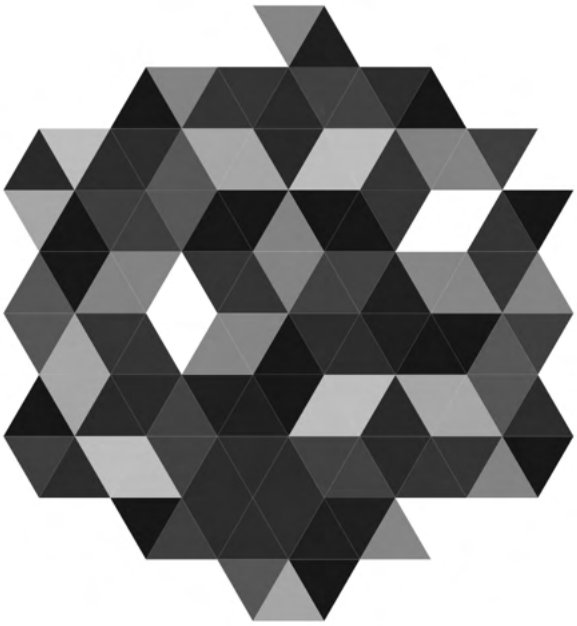

(b) "What the electron sees": Patch labelled by pairing type. This patch contains all 15 pairing types.

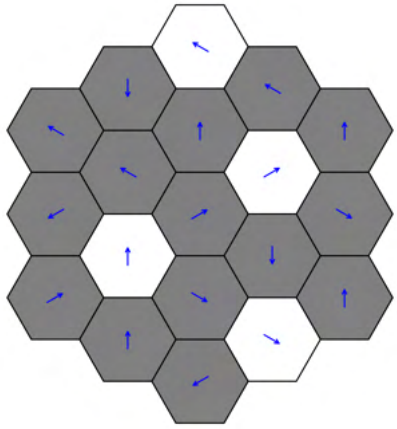

(c) Patch labelled by pairing type with arrows as described in Figure 14. This patch contains all 15 pairing types.

Figure 15: 19-tile test case for our ansatz. In (b), each metatile has 6 triangles overlaid on it such that each triangle matches with its neighbor metatile's triangle color. The color is mapped from weakest coupling (black) to strongest (white). This is possibly a new form of hexagonal Wang tiling.

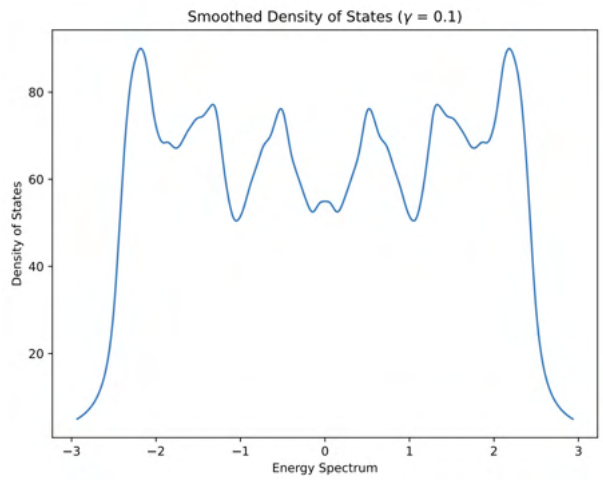

(a) Density of states of an example vertex model.

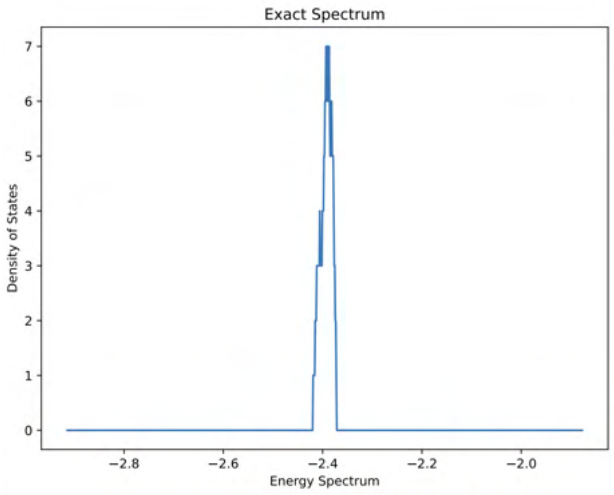

(b) Density of states of super-vertex model. We note that this is a very narrow Gaussian distribution.

Figure 16: Density of states of the 19-metatile patch in vertex and super-vertex forms.

Not surprisingly, the white diamonds in Figure 15b (the highest coupling energy in the super-vertex model) are combinatorially equivalent via the inflation rules to region around the four-coordinated vertices in the vertex model (the $\delta\pm$ connection). In both models, these highly coordinated and connected vertices dominate the wave functions and serve as an easy reference marker to orient oneself when looking at a patch.

Because the metatiles represent arbitrarily large sections of the vertices, this creates a self-similar wave function. According to Conway's theorem, in "a given local pattern in a region of some diameter l will be repeated within a distance of two diameters $2l$" (Rieth and Schreiber, 1998). Accordingly, these results seem to confirm the analysis in Rieth and Schreiber, 1998 that quasicrystal states are neither extended nor exponentially localized but obey a power-law drop off upon going between hierarchical levels, just as in the self-similarity we observe here.

1.7 Mid-Spectrum Analysis

As previously discussed, the relative lack of zero-modes compared to other bipartite aperiodic lattices seems to be a striking feature of the Spectre. As shown in Figure 19, zero-modes in the Spectre appear to be strongly localized and loosely resemble the zero-mode of the Γ tile (Figure 19a) but extended over a larger region. Less commonly, we observe an edge state such as in Figure 19b. In the largest patches we have studied, we have only observed a maximum of four zero-modes even with more than 11,000 vertices. We note that in all observed cases of exact zero-modes, the state is entirely on the B sublattice.

While the exact zero-modes appear to mainly be linear combinations of the Γ zero-modes, the near zero-modes exhibit string-like behavior stretching around the boundaries of many metatiles. Many examples of these strange near zero-modes can be seen in Figure 20. As can be verified in Figure 21, these near zero-modes are disproportionately on two-coordinated vertices, particularly on the edges between tiles in a narrow region around the zero-modes ($\sim -0.2t$ to $\sim 0.2t$). Note the large spike in the actual zero-modes on the center double weight corresponding to the Γ-like zero-modes seen in Figure 19c.

2 Physical Realization with Carbon Monoxide on Cu (111)

As demonstrated by Trainer et al., 2022, CO on Cu (111) can be used to explore topologically protected states in artificial lattices. Using this method, we hope to explore the synthesis of the Spectre tiling by examining the electronic states via local density of states (LDOS) measurements.

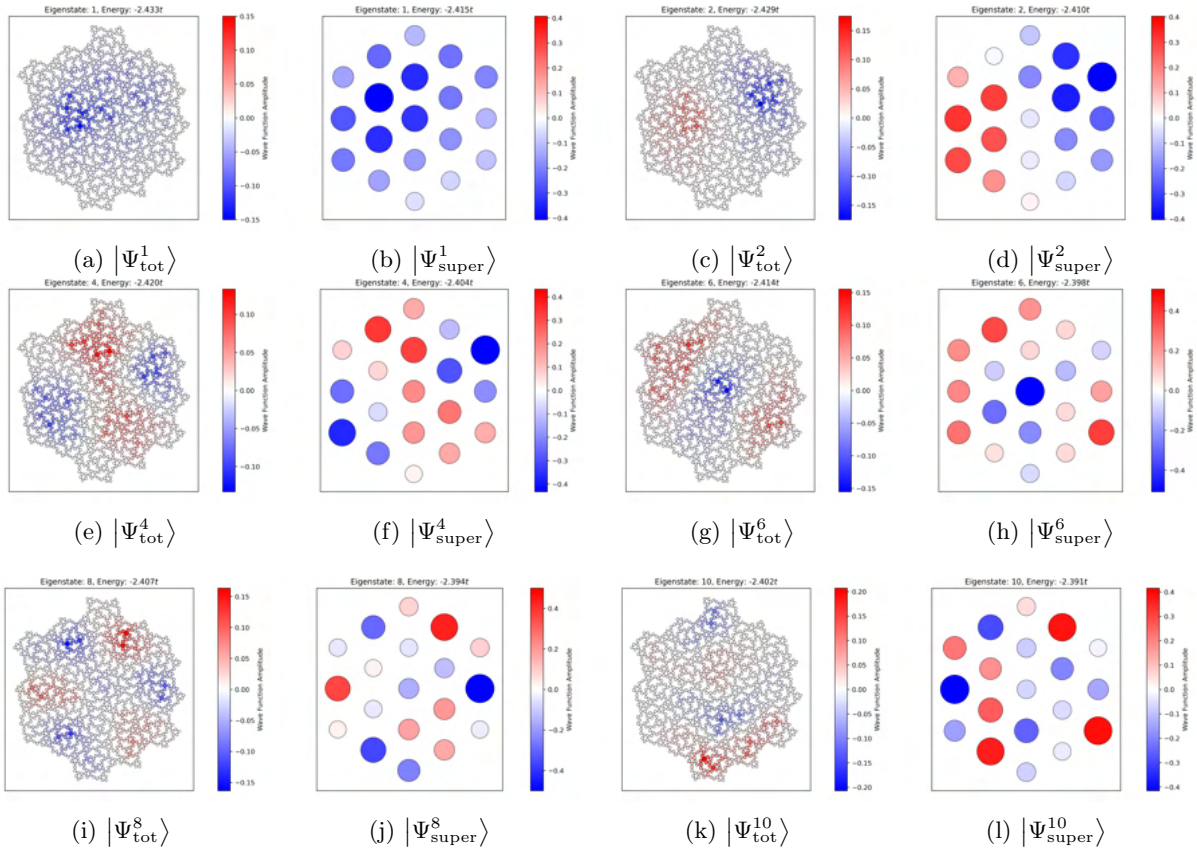

(a) $|\Psi^1_{\text{tot}}\rangle$ (b) $|\Psi^1_{\text{super}}\rangle$ (c) $|\Psi^2_{\text{tot}}\rangle$ (d) $|\Psi^2_{\text{super}}\rangle$

(e) $|\Psi^4_{\text{tot}}\rangle$ (f) $|\Psi^4_{\text{super}}\rangle$ (g) $|\Psi^6_{\text{tot}}\rangle$ (h) $|\Psi^6_{\text{super}}\rangle$

(i) $|\Psi^8_{\text{tot}}\rangle$ (j) $|\Psi^8_{\text{super}}\rangle$ (k) $|\Psi^{10}_{\text{tot}}\rangle$ (l) $|\Psi^{10}_{\text{super}}\rangle$

Figure 17: Wave functions of a 19-tile patch in both vertex and super-vertex models.

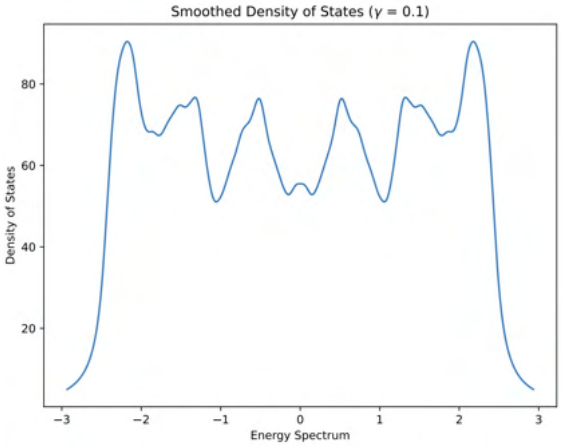

(a) Lorentzian Smoothing: 0.1

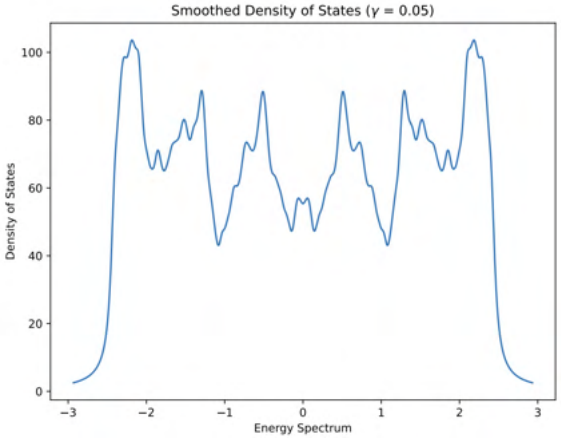

(b) Lorentzian Smoothing: 0.05

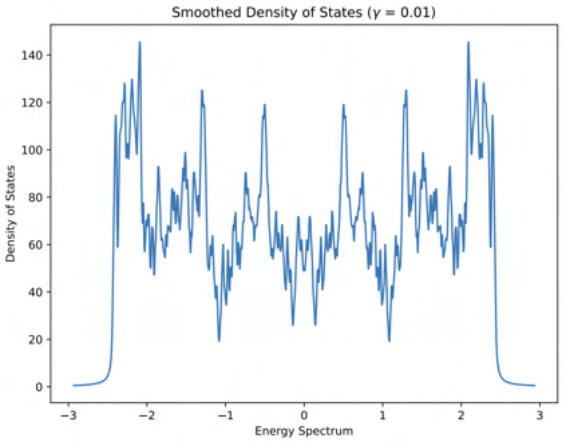

(c) Lorentzian Smoothing: 0.01

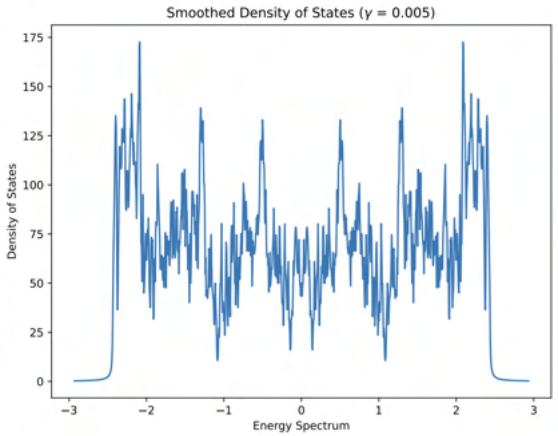

(d) Lorentzian Smoothing: 0.005

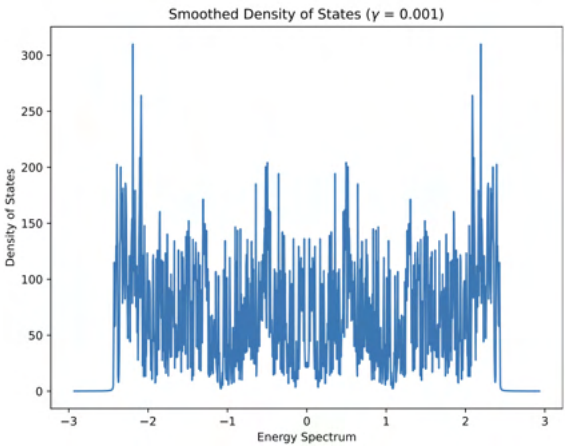

(e) Lorentzian Smoothing: 0.001

Figure 18: 19-tile Density of States at Different Smoothing Parameters.

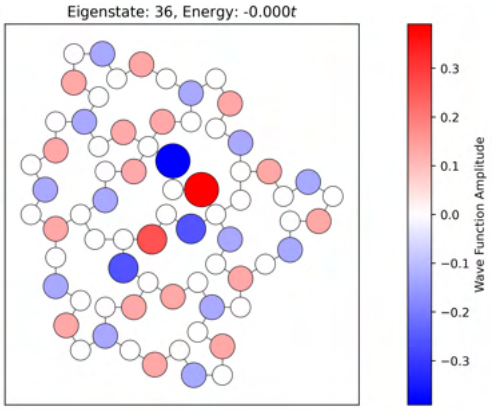

(a) The single zero-mode for the Γ tile. Note that it must have a zero-mode because of its odd vertices. The non-Γ tiles do not have any zero-mode.

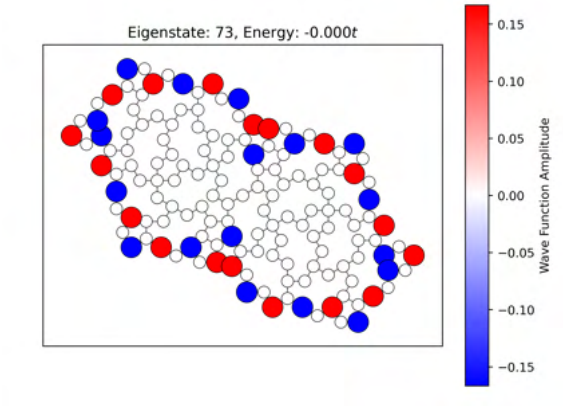

(b) The single zero-mode of a patch of two Ψ tiles. We have only observed pure edge states in certain patches of two tiles.

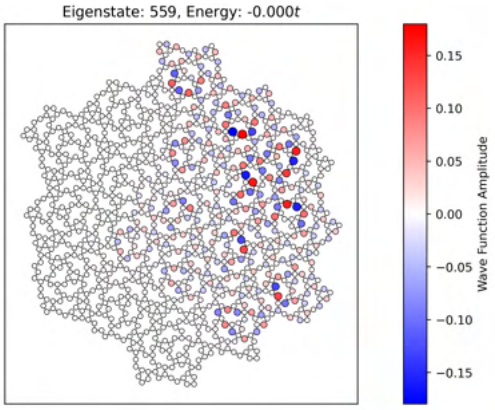

(c) One of three zero-modes in this patch of 19 tiles. Note how it appears that each tile is independently acting as a Γ tile in its excitation pattern.

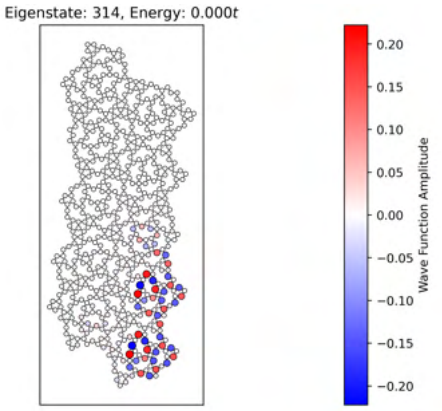

(d) One of two zero-modes for this strip of tiles. Despite having an even number of vertices, 628, it still exhibits two zero-modes.

Figure 19: Exact zero-modes across a variety of tiles.

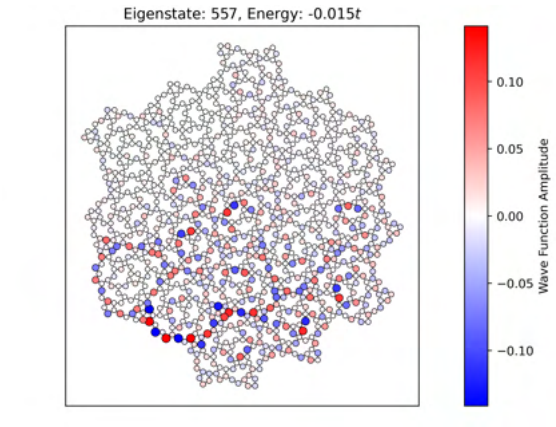

(a) One example of a near zero-mode in a patch of 19 tiles.

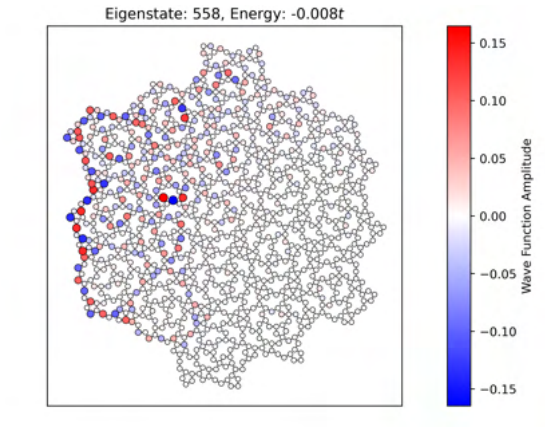

(b) Another example of a near zero-mode in a patch of 19 tiles.

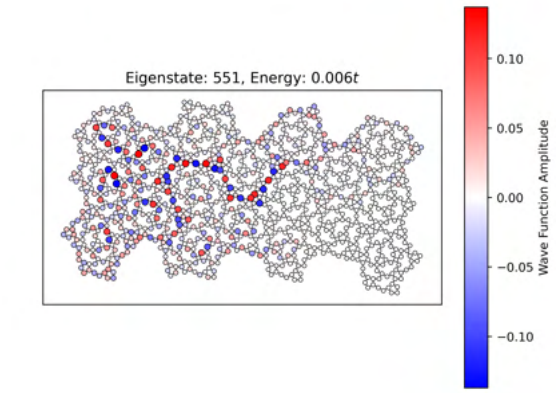

(c) An typical near zero-mode in a more irregularly shaped patch of tiles.

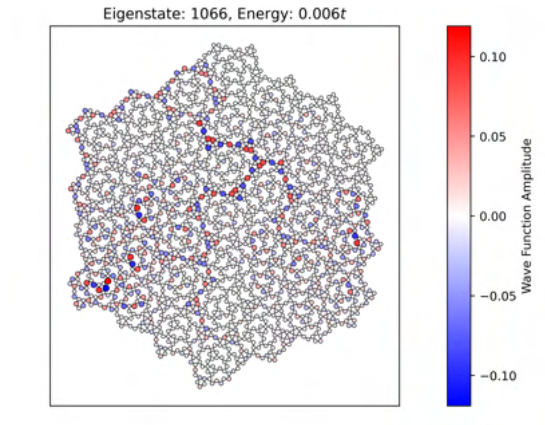

(d) A near zero-mode in a patch of 37 tiles.

Figure 20: Near zero-modes across a variety of tiles.

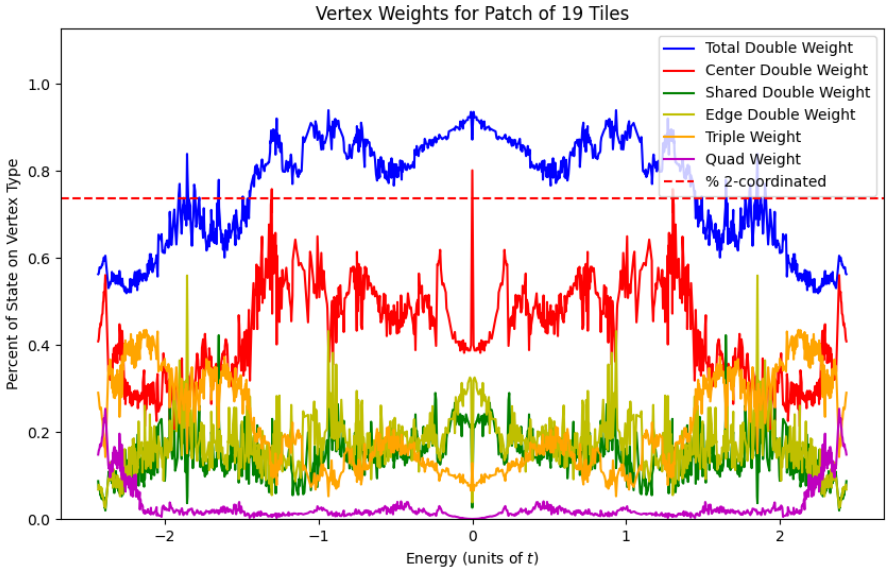

Figure 21: For the patch of 19 tiles analyzed previously, we compute the weight of each vertex type for each state n ($\sum_{i_{\text{type}}}^{N_{\text{type}}} |\langle i_{\text{type}} \,|\, \Psi_{\text{tot}}^n \rangle|^2$). "Shared Double" indicates that the vertex belongs to more than one tile (shown in dark blue in Figures 3b and 13a). "Edge Double" indicates the vertex lies on the outside of the patch and is not shared."Center Double" indicates the vertex is two-coordinated and is not on the edge of the tile. "Triple" and "Quad" indicate the coordination number of the vertex.

Using an artificial force field by trial and error, we first relax a set of circles (CO molecules) into a Spectre shape to get a rough filling. Here we use a chiral edge modification along the edges to help the "CO molecules" fit better into the shape. We then select only the circles along the edges and create one non-Γ meta-tile. Then, we overlay a hexagonal close-packed lattice with both ontop and FCC adsorption sites and snap each "CO molecule" to a site, placing in repulsion terms to aid in experimental reconstruction. The steps of this process can be seen in Figure 22.

TODO justify spacing, FCC and ontop etc

References

Arai, M., Tokihiro, T., Fujiwara, T., & Kohmoto, M. (1988). Strictly localized states on a two-dimensional penrose lattice. *Phys. Rev. B*, *38*, 1621–1626. https://doi.org/10.1103/PhysRevB.38.1621

Coates, S., Koga, A., Matsubara, T., Tamura, R., Sharma, H. R., McGrath, R., & Lifshitz, R. (2023). Hexagonal and trigonal quasiperiodic tilings.

Koga, A., & Coates, S. (2022). Ferrimagnetically ordered states in the hubbard model on the hexagonal golden-mean tiling. *Physical Review B*, *105*(10). https://doi.org/10.1103/physrevb.105.104410

Lee, J.-Y., & Moody, R. V. (2012). Taylor-socolar hexagonal tilings as model sets.

Matsubara, T., Koga, A., & Coates, S. (2023). Confined states in the tight-binding model on the hexagonal golden-mean tiling. *Journal of Physics: Conference Series*, *2461*(1), 012003. https://doi.org/10.1088/1742-6596/2461/1/012003

Rieth, T., & Schreiber, M. (1998). Numerical investigation of electronic wave functions in quasiperiodic lattices. *Journal of Physics: Condensed Matter*, *10*(4), 783.

Schirmann, J., Franca, S., Flicker, F., & Grushin, A. G. (2023). Physical properties of the hat aperiodic monotile: Graphene-like features, chirality and zero-modes.

Smith, D., Myers, J. S., Kaplan, C. S., & Goodman-Strauss, C. (2023). A chiral aperiodic monotile.

Socolar, J. E. S. (2023). Quasicrystalline structure of the smith monotile tilings.

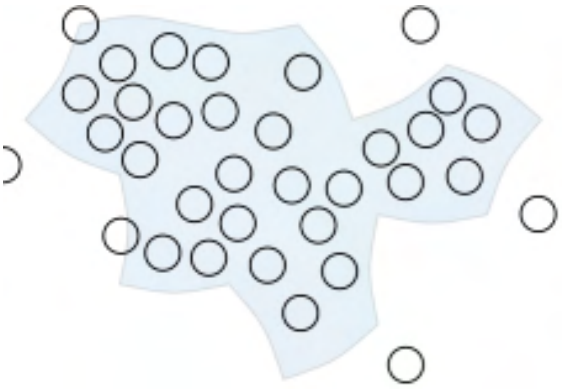

(a) 1. This frame depicts midway through the relaxation routine as the circles pack into the outline. They experience repulsion from each other and the walls once they are pushed inside the outline.

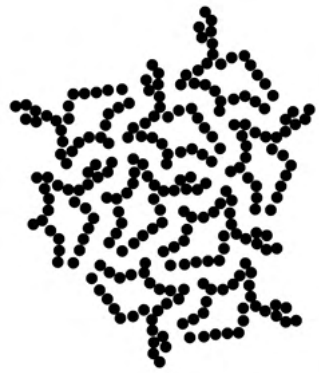

(b) 2. The inside circles are removed, and the structure is arranged in the form of a metatile.

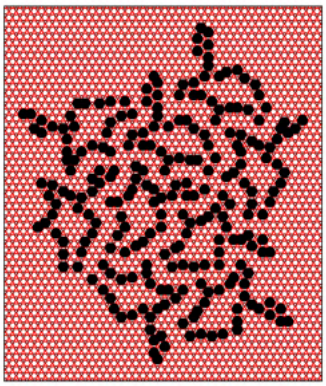

(c) 3. The circles are snapped to a grid with both ontop and FCC sites possible.

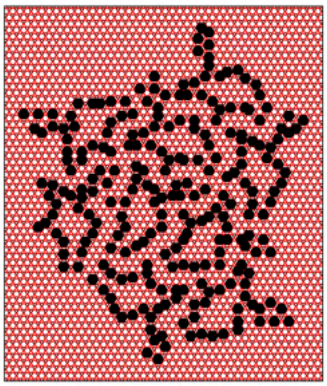

(d) 4. The "CO molecules" are relaxed once again to gain extra spacing on the lattice.

Figure 22: The steps for creating a layout of CO molecules on a Cu (111) surface.

Socolar, J. E., & Taylor, J. M. (2011). An aperiodic hexagonal tile. *Journal of Combinatorial Theory, Series A*, *118*(8), 2207–2231. https://doi.org/10.1016/j.jcta.2011.05.001

Trainer, D. J., Srinivasan, S., Fisher, B. L., Zhang, Y., Pfeiffer, C. R., Hla, S.-W., Darancet, P., & Guisinger, N. P. (2022). Artificial graphene nanoribbons: A test bed for topology and low-dimensional dirac physics. *ACS nano*, *16*(10), 16085–16090.